

Overview of diagnostic performance and results for the first operation phase in Wendelstein 7-X^{a)}

M. Krychowiak,^{1,b)} A. Adnan,¹ A. Alonso,⁶ T. Andreeva,¹ J. Baldzuhn,¹ T. Barbui,⁷ M. Beurskens,¹ W. Biel,² C. Biedermann,¹ B. D. Blackwell,¹⁸ H. S. Bosch,¹ S. Bozhnikov,¹ R. Brakel,¹ T. Bräuer,¹ B. Brotas de Carvalho,³ R. Burhenn,¹ B. Buttenschön,¹ A. Cappa,⁶ G. Cseh,⁴ A. Czarnecka,⁵ A. Dinklage,¹ P. Drews,² A. Dzikowicka,¹⁹ F. Effenberg,⁷ M. Endler,¹ V. Erckmann,¹ T. Estrada,⁶ O. Ford,¹ T. Fornal,⁵ H. Frerichs,⁷ G. Fuchert,¹ J. Geiger,¹ O. Grulke,¹ J. H. Harris,¹³ H. J. Hartfuß,¹ D. Hartmann,¹ D. Hathiramani,¹ M. Hirsch,¹ U. Höfel,¹ S. Jabłoński,⁵ M. W. Jakubowski,¹ J. Kaczmarczyk,⁵ T. Klinger,¹ S. Klose,¹ J. Knauer,¹ G. Kocsis,⁴ R. König,¹ P. Kornejew,¹ A. Krämer-Flecken,² N. Krawczyk,⁵ T. Kremeyer,⁷ I. Książek,¹⁴ M. Kubkowska,⁵ A. Langenberg,¹ H. P. Laqua,¹ M. Laux,¹ S. Lazerson,¹⁰ Y. Liang,² S. C. Liu,² A. Lorenz,¹ A. O. Marchuk,² S. Marsen,¹ V. Moncada,⁸ D. Naujoks,¹ H. Neilson,¹⁰ O. Neubauer,² U. Neuner,¹ H. Niemann,¹ J. W. Oosterbeek,⁹ M. Otte,¹ N. Pablant,¹⁰ E. Pasch,¹ T. Sunn Pedersen,¹ F. Pisano,¹⁵ K. Rahbarnia,¹ L. Ryć,⁵ O. Schmitz,⁷ S. Schmuck,¹⁶ W. Schneider,¹ T. Schröder,¹ H. Schuhmacher,¹¹ B. Schweer,² B. Standley,¹ T. Stange,¹ L. Stephey,⁷ J. Svensson,¹ T. Szabolics,⁴ T. Szepesi,⁴ H. Thomsen,¹ J.-M. Travers,⁸ H. Trimino Mora,¹ H. Tsuchiya,¹⁷ G. M. Weir,¹ U. Wenzel,¹ A. Werner,¹ B. Wiegel,¹¹ T. Windisch,¹ R. Wolf,¹ G. A. Wurden,¹² D. Zhang,¹ A. Zimbal,¹¹ S. Zoletnik,⁴ and the W7-X Team^{c)}

¹Max Planck Institute for Plasma Physics, 17491 Greifswald, Germany

²Institute of Energy- and Climate Research, Forschungszentrum Jülich GmbH, D-52425 Jülich, Germany

³Instituto de Plasmas e Fusão Nuclear, Av. Rovisco Pais 1, 1049-001 Lisboa, Portugal

⁴Wigner Research Centre for Physics, Konkoly Thege 29-33, H-1121 Budapest, Hungary

⁵Institute of Plasma Physics and Laser Microfusion, Hery Street 23, 01-497 Warsaw, Poland

⁶Laboratorio Nacional de Fusión, CIEMAT, Avenida Complutense, Madrid, Spain

⁷Univ. of Wisconsin, Engineering Drive, Madison, WI 53706, USA

⁸CEA, IRFM, F-13108 Saint-Paul-lez-Durance, France

⁹Eindhoven University of Technology, P.O. Box 513, 5600 MB Eindhoven, The Netherlands

¹⁰Princeton Plasma Physics Laboratory, Princeton, New Jersey 08543, USA

¹¹Physikalisch-Technische Bundesanstalt, Bundesallee 100, 38116 Braunschweig, Germany

¹²Los Alamos National Laboratory, Los Alamos, NM 87544, USA

¹³Oak Ridge National Laboratory, Oak Ridge, Tennessee 37831, USA

¹⁴Opole University, pl. Kopernika 11a, 45-040 Opole, Poland

¹⁵University of Cagliari, Via Università, 40, 09124 Cagliari, Italy

¹⁶Culham Science Centre, Abingdon, OX14 3DB, United Kingdom

¹⁷NIFS National Institute for Fusion Science, 322-6 Oroshi-cho, Toki, 509-5292 Japan

¹⁸Australian National University, Acton ACT 2601, Canberra, Australia

¹⁹University of Szczecin, al. Papieża Jana Pawła II 22A, Szczecin, Poland

Wendelstein 7-X, a superconducting optimized stellarator built in Greifswald/Germany, started its first plasmas with the last closed flux surface (LCFS) defined by 5 uncooled graphite limiters in December 2015. At the end of the 10 weeks long experimental campaign (OP1.1) more than 20 independent diagnostic systems were in operation, allowing detailed studies of many interesting plasma phenomena. For example, fast neutral gas manometers supported by video cameras (including one fast-frame camera with frame rates of tens of kHz) as well as visible cameras with different interference filters, with field of views covering all ten half-modules of the stellarator, discovered a MARFE-like radiation zone on the inboard side of machine module 4. This structure is presumably triggered by an inadvertent plasma-wall interaction in module 4

resulting in a high impurity influx that terminates some discharges by radiation cooling. The main plasma parameters achieved in OP1.1 exceeded predicted values, revealing electron temperatures ≤ 10 keV, ion temperatures ≤ 2 keV and electron densities $\leq 5 \times 10^{19} \text{ m}^{-3}$, in discharges of a length reaching 6 seconds. Although OP1.1 is characterized by short pulses, many of the diagnostics are already designed for quasi-steady state operation of 30 minute discharges heated at 10 MW of ECRH. An overview of diagnostic performance for OP1.1 is given, including some highlights from the physics campaigns.

^{a)} Invited paper published as part of the Proceedings of the 21st Topical Conference on High-Temperature Plasma Diagnostics (HTPD 2016) in Madison, Wisconsin, USA.

^{b)} Author to whom correspondence should be addressed: cak@ipp.mpg.de

^{c)} Members of the W7-X Team are listed in Nucl. Fusion **53** (2013) 126001.

I. INTRODUCTION

Wendelstein 7-X (W7-X) – a new fusion experiment of stellarator type – has been successfully commissioned in 2015. Its superconducting coil system provides continuous magnetic field, a prerequisite for proving the steady state capability of this optimized stellarator. The first experimental campaign [1] started in December 2015 and lasted for three months, featuring ~ 1000 plasma discharges. The main purpose of this campaign was the integral commissioning of the machine and diagnostics, which was reached very well. The LCFS of the plasma was defined by 5 poloidal uncooled graphite limiters at the inboard side of the plasma vessel, shaped in a way to conform along its entire length to the edge plasma for the standard iota configuration and to receive the full convective heat load from the plasma. The initially set maximum of 2 MJ (ECR) heating power per discharge has been extended to 4 MJ in the course of OP1.1 because of lower than expected convective heat loads to the limiters. This was caused partially by significant fraction of the heating power being radiated away from the plasma edge as consequence of strong wall outgassing.

More than 20 diagnostic systems have been installed [2], commissioned and almost in all cases successfully operated during OP1.1, allowing many physics investigations. This paper gives an overview of the diagnostics with the exception of the neutron counters [3], ECRH sniffer probes [4], a very comprehensive set of magnetic probes [5], a Doppler and a correlation reflectometer [6,7,8], a single line of sight (los) Z_{eff} measurement and an overview UV-VIS spectrometer. Some details of their design (the capability of long pulse plasma operation [9,10] is emphasized if available), their performance and example results from OP1.1 are presented. In addition the Bayesian inference based Minerva framework used for data analysis of several W7-X diagnostics is briefly discussed.

II. DIAGNOSTIC SET FOR THE FIRST OPERATION PHASE OF W7-X

A. Measurement of magnetic flux surfaces

One of the optimization criteria at W7-X is related to the existence of good closed and nested magnetic flux surfaces in a wide configuration space. In stellarator like magnetic configurations the verification of the existence and quality of magnetic flux surfaces is possible for the vacuum case i.e. without the existence of a plasma. The diagnostic comprises two 5 m long vacuum plug-ins with fluorescent swiveling rods in the plasma vessel serving a probing electron beam whose trajectory is optically detected inside the confinement area either due to

interaction with background gas in the plasma vessel or due to fluorescence light emission by the electrons hitting the rod. The manipulators can be retracted in the port behind water cooled shutters to sustain steady state plasma discharges.

First flux surface measurements have been performed for the standard OP1.1 magnetic configuration up to a magnetic field of 2.5 T. The experiments that have been conducted before the first plasmas confirmed the existence of closed flux surfaces from the magnetic axis up to the limiter. In addition expected intrinsic magnetic island chain at $\iota=n/m=5/6$ inside the confinement region has been detected [11]. As modelled by finite element analysis the electromagnetic forces are causing an elastic deformation of the non-planar field coils depending on the field strength, thus influencing the rotational transform and hence the radial position of that island chain as well. That radial shift of the islands which is of the order of a few cm has been detected in the experiments.

Further experiments were dedicated to the estimation of error fields. For an $\iota=n/m=1/2$ configuration and at low magnetic field of 0.3 T the B_{21} Fourier harmonic error field has been derived from the finite width of a non-natural island found at this resonance. The initial analysis is indicating that the relative b_{21} error field component is of the order of $<1 \times 10^{-5}$ and seems to be caused by tolerances in the manufacturing and assembly of the magnetic field coils. Further error field experiments (especially including the most severe 1/1 component) will be conducted before the next operation campaign.

B. Diagnostics for plasma profiles

A multi-pulse Nd:YAG laser **Thomson scattering system** is installed at W7-X as a powerful diagnostic for electron temperature and density measurements [12] (for measurement of T_e profiles with the XICS diagnostic see section D). In OP1.1 a reduced set of 10 fiber bundles was installed to cover a half profile of the plasma cross section, as shown in FIG. 1. The optics is placed in a water cooled immersion tube designed for long pulse operation with a vacuum window protected against coating by a water cooled shutter. Interference filter based polychromators are used for detection of the scattered light. Fast and high dynamic range ADCs (1 GS/s, 14 bit) digitize the signals from Si-avalanche diodes. The Thomson scattering system is optimized to measure electron temperatures in the range of 20 eV to 10 keV.

A **single channel dispersion interferometer** has been installed for measurement of the line integrated density [13]. It is based on a 20W CO₂ laser and its second harmonic generated in a AgGaSe₂ frequency doubling crystal. Both beams pass the plasma vessel twice being reflected by a corner cube reflector which is located outside the vacuum vessel at an opposite port. A separate reference path is not required. After frequency doubling the residual 10.6 μm beam is frequency doubled in a second AgGaSe₂ crystal, the phase shift of the 5.3 μm signals being detected. Dispersion interferometers are intrinsically insensitive to vibrations along the optical beam path, only vibrations perpendicular to that path increase the phase noise. The phase

measurement uses a heterodyne modulation scheme applying a photoelastic ZnSe modulator (PEM) at a modulation frequency of 50 kHz which also determines the temporal resolution. The single channel dispersion interferometer shares its sightline with the Nd:YAG laser of the Thomson scattering system, therefore cross-calibration of both systems can be performed easily. The diagnostics were operated routinely during the first operation campaign. FIG. 2 shows a comparison of the line integrated density measured with the interferometer and derived from the Thomson scattering profiles.

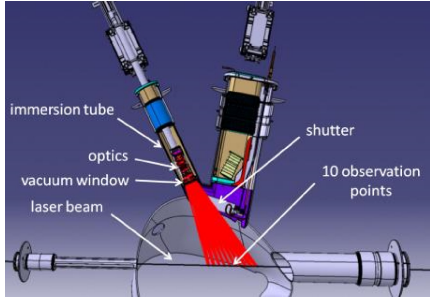


FIG. 1. (Color online) Main components of the Thomson scattering system.

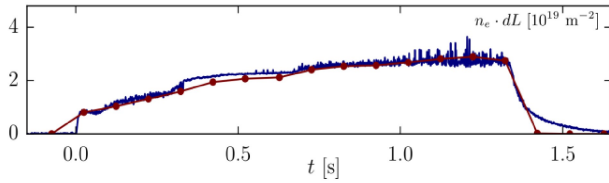


FIG. 2. (Color online) Time trace of the line integrated electron density measured with the interferometer (blue line) and derived from the Thomson scattering profiles (red dots), pulse 160308007.

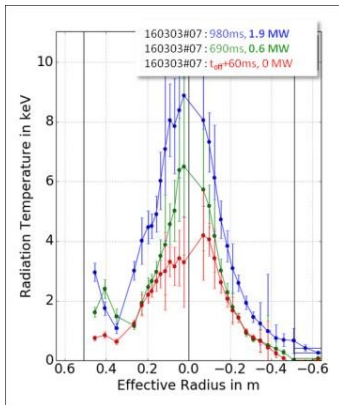


FIG. 3. (Color online) T_e profiles from ECE of a discharge with ECRH power steps: 1.9 MW (blue), 0.6 MW (green) and 60 ms after the termination of the heating (red). Vertical bars reflect the absolute calibration uncertainties of the individual channels.

An **Electron Cyclotron Emission** diagnostic (ECE) has been operated throughout OP1.1 as the main tool to study electron heating by ECRH and subsequent electron heat transport. It measures the 2nd harmonic X-mode emission in the frequency band 126 GHz to 162 GHz along a sightline defined by Gaussian optics with a 32-channel heterodyne radiometer located outside the torus hall [14]. Microwave stray radiation resulting from non absorbed ECRH power is cut out of the spectrum by a 1

GHz wide waveguide Bragg reflection notch filter with depth >40 dB showing extremely steep edges and an insertion loss of only 3 to 5 dB outside this frequency band [15]. The radiometer is absolutely calibrated by a second identical Gaussian optical system built as a twin outside the torus including identical waveguide components, mica window and a geometrically identical transmission line, however with a hot-cold calibration source chopping between LN_2 and room temperature in front of it. The overall absolute calibration error is $\sim 10\%$ with outliers for individual channels resulting from their detection sensitivity (see example in FIG. 3). T_e profiles are derived from the X2 emission spectra taking into account the finite optical thickness via the ray-tracing code TRAVIS which implies a fully-relativistic model of EC absorption and emission. First comparison with T_e profiles obtained from Thomson scattering and imaging X-ray spectroscopy yields good agreement.

C. Diagnostics for plasma edge and in-vessel components

The overview **video diagnostic system** is mounted in ten tangential ports of W7-X giving a good toroidal coverage [16]. A dedicated docking mechanism allows fast insertion of each channel in its respective port from outside the machine. Water cooled front ends with a pin hole provide sufficient protection from the heat load and coating in long pulse plasma operation. Three different camera types are used. The standard system for regular monitoring of mostly the plasma shape, size and the radiation distribution is equipped with 7 EDICAM cameras (~ 400 frames/s @ 1.3Mpixel). The EDICAM system features FPGA-based real-time image processing and event detection, to be utilized in the forthcoming campaigns of W7-X. 2 PCO PixelFly cameras (12 frames/s @ 1.3 Mpixel) are used for the vacuum magnetic flux surface measurements, and one tangential channel is equipped with an image guide attached to a fast framing camera (Photron SA5, 7 kframes/s @ 1 Mpixel).

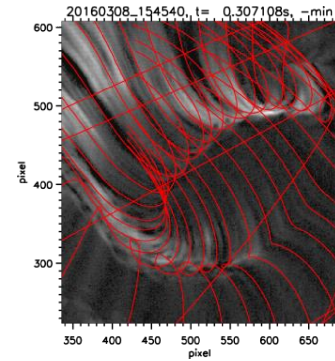


FIG. 4. (Color online) Short exposure (~ 20 μs) background corrected tangential image showing field line aligned structures. Calculated vacuum field lines are over plotted in red.

The EDICAM system revealed toroidal or poloidal asymmetries as well as the movement of the plasma as reaction to currents applied in trim coils inducing 1/1 magnetic field errors. Taking images at a frame rate greater than a few kHz with the Photron camera, filamentary structures at the plasma edge have been detected, usually at later phases of the discharges accompanied by strong edge radiation or in case of intentional gas injection used for radiative edge cooling experiments. These structures are aligned to the magnetic field lines (FIG. 4), are extended toroidally in the whole observation volume of the camera, having in some cases a lifetime of a few milliseconds and revealing poloidal rotation.

The **neutral gas density measurement** was performed by five in-vessel pressure gauges of the ASDEX type [17] and one Penning gauge [18]. The pressure gauges were placed at front-ends of vacuum plug-ins at the midplane outboard side in all five stellarator modules for investigations of the toroidal symmetry. The usage of the vacuum plug-in technique has different advantages: the possibility of rapid change of the manometer position, exchange for repair and of water cooling for steady state operation (to be implemented for the next campaign). The measurement range spans almost five orders of magnitude from 2×10^{-7} up to 1×10^{-2} mbar, with maximum sampling rate of 2 kHz. In FIG. 5 a strong asymmetry of the neutral gas pressure is shown in a discharge terminated by too high edge radiation. Only in module 4 the gas pressure rises from the beginning of the discharge reaching a highly peaked value and is in some cases accompanied by a MARFE-like radiation on the inboard side of module 4 detected by the video cameras [19].

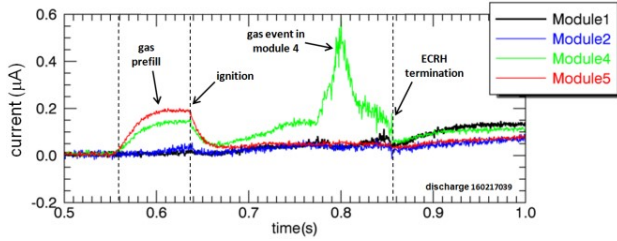


FIG. 5. (Color online) Neutral gas pressure in four machine modules in a discharge terminated by strong edge radiation.

Several **cameras for observation of the limiters and the walls** have been installed, among them infrared cameras to measure temperature distribution on the limiter surfaces. Three types of cameras have been used: NIR cameras (measuring at 0.9 μm , installed in immersion tubes mentioned later in this chapter), one MWIR camera (measuring at 3-5 μm , viewing the limiter in module 3) and one LWIR camera (measuring at 10-14 μm , viewing the limiter in module 5). The data from NIR cameras suffered from plasma emission near the limiter surface. However MWIR and LWIR cameras delivered very useful data. In FIG. 6(a) temperature distribution on the limiter in module 5 measured with the LWIR camera is shown. The topology of magnetic field lines is more complicated than in tokamaks with its 3D structure of inter-woven flux tubes. This is reflected in temperature distribution, which also shows 3D characteristics.

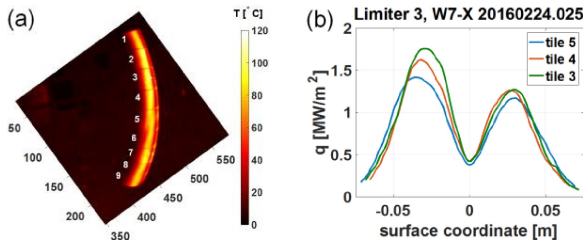


FIG. 6. (Color online) (a) Infrared image of limiter in module 5 shows heterogeneous temperature distribution due to 3D structure of the scrape-off layer; (b) Heat flux density profiles calculated at three tiles of limiter in module 3.

The MWIR camera shared the same field of view at the limiter in module 3 with a visible camera [20]. The limiter was seen with high temporal resolution (~ 400 Hz in the IR and ~ 100 Hz in the visible) and sub-mm spatial resolution on five of its nine tiles. The filtered visible camera provided absolutely calibrated measurements of carbon and hydrogen light, and

therefore inputs to particle balance calculations [21]. The infrared camera was used to derive space and time resolved power fluxes, as well as in a calorimeter mode to infer total energy deposited on the limiter. From the thermographic measurements of limiter temperatures, heat flux density has been derived with the help of the THEODOR code [22]. For a typical discharge of the first campaign with 3 MW of injected power, there is about 1.5 MW/m^2 heat flux near the watershed (see FIG. 6(b)). These values are lower than expected due to high fraction of radiated power during the operation which allowed increasing the limit of heating energy from 2 MJ to 4 MJ per plasma pulse.

FIG. 7 shows two limiter images taken with the visible camera in module 3. In Fig. (a) a carbon bloom emission from a hot spot defect is shown, and in Fig. (b) measured absolute H_α emission at the limiter providing particle fluxes is depicted.

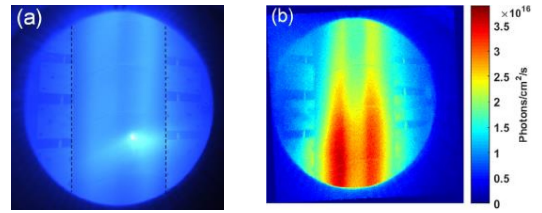


FIG. 7. (Color online) (a): 465 nm CIII light showing a carbon bloom observed from a hot spot defect on the limiter in module 3 (black lines indicate the limiter edges). (b): H_α light at the limiter detected by the same camera (discharge 160308032 at 120 ms).

For the observation of the divertor region (in upcoming operation phase) and the limiter in OP1.1 10 **immersion tubes with NIR and visible cameras** are installed. Each tube is equipped with a set of three cameras, two operating in the visible spectral range with various interference filters (H_α , CII, and CIII) and one NIR camera. The viewing angle of 86° to 136° allows the monitoring of a wide range of the plasma vessel interior with a spatial resolution of 4 to 10 mm. During the first operation phase OP1.1 the visible radiation patterns at the limiters were dominated by hydrogen and carbon emission. In FIG. 8 CIII emission is shown revealing the typical double-stripe structure (compare to H_α emission in FIG. 7(b)).

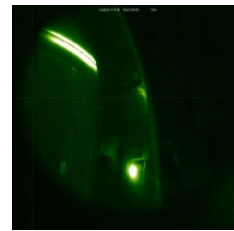


FIG. 8. CIII emission at limiter in module 5 (double-stripe structure at top left) detected with a visible camera and an interference filter at 467 ± 5 nm. The bright spot at bottom right is due to NeI emission from neon injected by the helium beam injection system for edge cooling experiments.

The IR and visible cameras have been complemented by an absolutely calibrated **filterscope system** [23] to obtain spectroscopic data of limiter and first wall recycling and impurity sources. A fiber view with a spot size encompassing the width of the limiter (16 cm) provides simultaneous measurements at the limiter in module 3 of HeI , H_α , H_β , and CII emission. These measurements have excellent temporal resolution of 10 microseconds and cover a large subset ($\sim 50\%$) of the same area as the visible camera views. Four other fiber views of the inboard

and outboard wall detected additional H, HeI, HeII, and C emission, as well as visible bremsstrahlung at 523 nm. The HeII emission decay, shown in FIG. 9, was used to determine the τ_p^* (particle confinement time including recycling effects) for helium from a series of perturbative helium puffs that were designed to assess changes in particle confinement. The resulting photon flux from both the visible camera and filterscopes can then be compared to an EMC3-EIRENE synthetic diagnostic [24] output to infer both the limiter and the wall particle flux, which will ultimately be used to infer a complete particle balance.

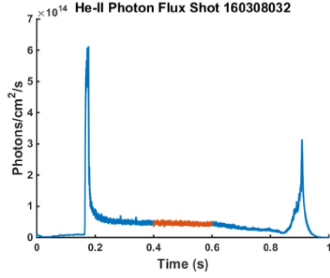


FIG. 9. (Color online) HeII emission detected by the filterscope viewing the limiter in module 3. τ_p^* He is derived from the time decay of the emission (red line) after a He puff at ~200 ms.

For the gas injection of the **thermal helium beam** two water cooled vacuum plug-ins capable of steady state plasma operation – one for the upper and one for the lower plasma edge – have been operated during OP1.1. Both were equipped with a valve box with five independent fast piezo valves [25] positioned only few cm outside of the LCFS (FIG. 10). The versatile gas injection system has been used for injection of helium for measurement of local edge n_e and T_e profiles [27] and effective particle confinement time τ_p^* He [21], neon for development of a collisional radiative model to extend the parameter range and accuracy of the diagnostic helium beam [27,28], argon for impurity transport studies as well as nitrogen for radiative edge cooling. Perpendicular observation of the gas emission at the upper plasma edge was done along 8 los, using quartz fibers and an imaging spectrometer with a CCD camera [27].

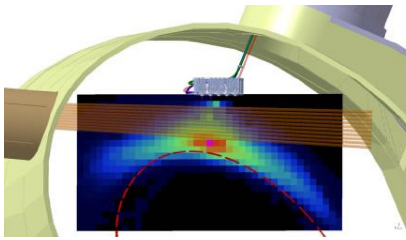


FIG. 10. (Color online) Geometry of the helium beam diagnostic at the upper plasma edge. Adjustment of the 8 los was supported by the shown EMC3-EIRENE simulation of HeI emission at 706 nm [26]. The LCFS is indicated by the dashed red line.

A **multipurpose manipulator with a fast reciprocating probe** has been assembled at the outboard side near to the equatorial plane. Two probe heads were available: a combined probe measuring the edge plasma profiles or fluctuations (at fixed probe position) as well as a sample station for plasma exposure studies of different materials. The probes equipped with water cooling are capable of steady state plasma operation. The manipulator is able to plunge as far as 350 mm into the plasma vessel and thereby easily through the LCFS. The combined probe includes two magnetic pick-up coil arrays, Langmuir probes, and a Mach setup. This allows measuring at the same time and

location, the edge radial profiles of the magnetic fields, the electron temperature and density, the electric fields and the plasma flows [29]. The Langmuir probes are operated in a triple probe configuration providing high temporal resolution and easy calculation of the temperature and density. The **limiter Langmuir probes** comprise two arrays with 20 probes each installed in two tiles of the limiter in module 5. The probes provided different measures at 2 ms time resolution at the limiter surface. They measured either the floating potential and the ion saturation current at constant bias voltage of -100 V or have swept the voltage between -100 V and 10 V for measurement of n_e and T_e , detecting values up to $1 \times 10^{19} \text{ m}^{-3}$ and 5-70 eV, respectively. FIG. 11 shows a result of plasma edge cooling by pulsed N_2 puffs through the helium beam injection system at the lower plasma edge in module 3. There is a clear correlation of the injection time and the T_e values measured both by the manipulator probe (at fixed position in this experiment) in module 4, and by some probes at the limiter (measuring outside of the LCFS) in module 5. The indicated time delay of ~10 ms is at least partially due to the opening time of the piezo valve.

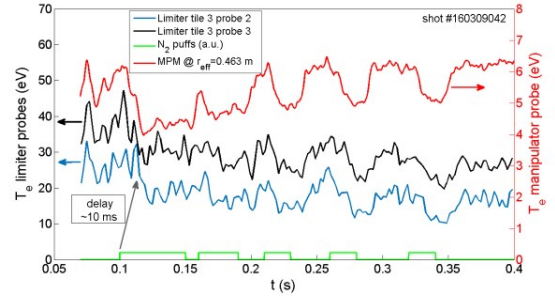


FIG. 11. (Color online) Cooling of the plasma edge detected with Langmuir probes at different positions in the plasma vessel as reaction on N_2 injection into the edge plasma.

D. Diagnostics for core impurities

The imaging spectrometer systems **X-ray Imaging Crystal Spectrometer** (XICS) [30,31,32] and **High Resolution X-ray Imaging Spectrometer** (HR-XIS) [33], perform complementary measurements of the spectral emission of selected impurities in different charge states, yielding radial profiles of ion and electron temperature, plasma flow velocity, and impurity densities with a time resolution of 5 ms. Both spectrometers have been commissioned during OP1.1.

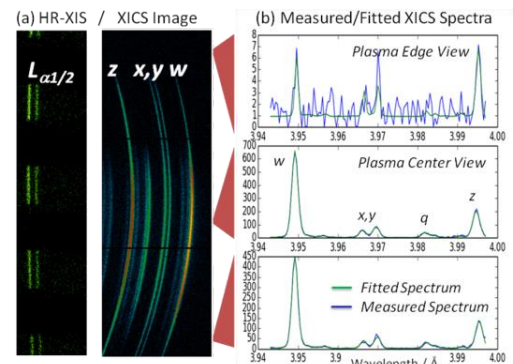


FIG. 12. (Color online) (a) HR-XIS and XICS raw images of ArXVIII and ArXVII emission. (b) Measured and fitted XICS spectra along los crossing the plasma at the top edge, the center and below the magnetic axis (plots top to bottom, respectively).

In those spectrometers, X-rays emitted from the plasma are imaged via a spherical bent crystal onto a 2D detector unit with energy resolution in horizontal and spatial resolution in vertical direction. FIG. 12(a) shows typical 2D intensity patterns of ArXVIII ($L_{\alpha 1/2}$ lines) and ArXVII (w, x, y , and z lines) emission after injection of trace amounts of argon ($n_{Ar}/n_e \sim 2 \times 10^{-4}$) into the plasma. A spectral fit (green line in FIG. 12(b)) of los integrated, measured spectra (blue line in FIG. 12(b)) and a tomographic inversion yield profiles of above mentioned plasma parameters as shown in FIG. 13. Here, temperature and density profiles have been inferred using an entire forward model of the XICS system within the Minerva Bayesian analysis framework [34]. First results of the evolution of plasma flow velocity profiles [35] and argon impurity transport studies [36] using XICS data are discussed in the given references.

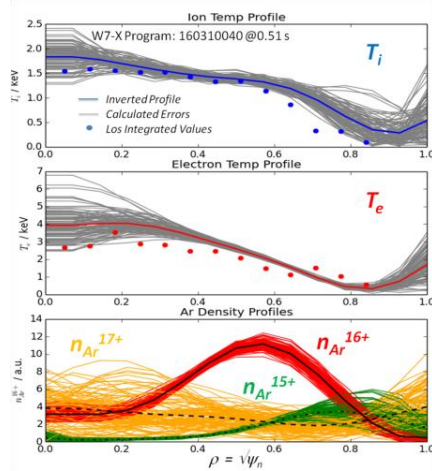


FIG. 13. (Color online) Inferred local ion and electron temperature (thick solid lines) as well as argon density profiles of different charge states (thick solid, dashed and dash-dotted lines) including samples from posterior probability distribution (thin solid lines); los integrated temperatures are shown with dots.

As one of the main impurity diagnostics, the **High Efficiency XUV Overview Spectrometer** (HEXOS) [37,38,39] covers the VUV/XUV wavelength region between 2.5 and 160 nm, distributed over four spectral channels, with high spectral and temporal (up to 1000 spectra/s) resolution along two almost identical los going through the plasma center. The most intense resonance lines of medium ionization stages of expected intrinsic impurities as well as injected tracer impurities (e.g. argon, neon, nitrogen) emit light at wavelengths covered by HEXOS.

FIG. 14 shows overview spectra of the lowest energy channel of HEXOS for three different discharge scenarios. Positions of identified emission lines are marked. Clearly identifiable are oxygen and carbon lines in all cases, as well as argon lines for the discharge with argon prefill. All spectra also contain emission lines of fluorine and chlorine, and indications of sulphur.

The **Pulse Height Analysis** (PHA) system [40,41] is used for investigation of soft X-ray emission in the energy range from 250 eV to 20 keV. It consists of 3 energy channels equipped with Silicon Drift Detectors (SDDs). Each SDD is filtered by a thin foil (Be or Polymer) and accompanied by a pulsed-reset preamplifier and individual power supply module in order to avoid electric interaction between detection channels. Each energy channel is equipped with a set of changeable piezo-slits (0-1.2 mm) and additional exchangeable Be foils (10-500 μ m) to assure appropriate flux of X-rays under different discharge

conditions. The main purpose of the diagnostic is to identify spectral lines emitted by impurities in the plasma [39] as well as estimate the electron temperature and suprathermal electron distribution from the continuum radiation. During OP1.1 the PHA system was launched and tested. Two example spectra detected by the 1st energy channel (SDD with 8 μ m and 25 μ m Be foil) are presented in FIG. 15.

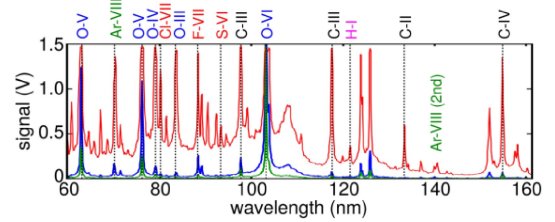


FIG. 14. (Color online) HEXOS spectra (spectrometer 4) of three different discharge scenarios (green: no argon prefill, blue: with argon prefill, red: with argon prefill during radiation collapse).

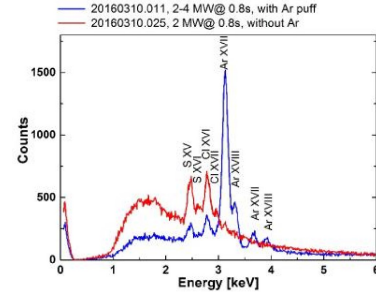


FIG. 15. (Color online) Integrated spectra from two discharges with (blue) and without (red) argon prefill (same as in FIG. 14).

Two endoscopes with horizontal and vertical **bolometer** cameras based on metal-resistive detectors have been operated during OP1.1 [42,43]. Special efforts have been undertaken to prepare the diagnostic for steady state operation of W7-X. The aperture plates and detector holders are water cooled as protection from thermal overheating as well as to minimize thermal drifts of the detector offset. Metal meshes mounted in front of the detectors in addition to ceramic absorber layers coated on the inner side of the detector enclosures suppress the EC stray radiation in the detector chamber by factor of 300. Pneumatically driven shutters protect the detectors from contamination during machine conditioning as well as for offset measurements and in-situ calibrations even during long pulse plasma operation.

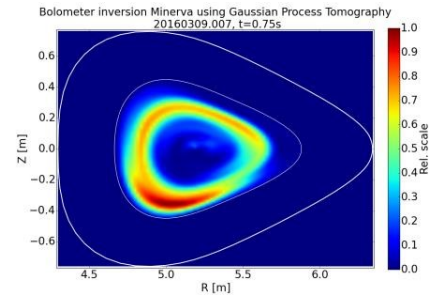


FIG. 16. (Color online) Tomographic inversion of bolometer signals using Gaussian Process Tomography [44].

During OP1.1, no microwave interference on the detected signals has been observed. Total radiative power losses from the plasma of 25-40% of the heating power (being varied in different experiments) have been derived from the signals of the horizontal bolometer camera. In FIG. 16 reconstructed 2D emission of a hydrogen plasma with a strong radiation zone at the outer radial region is shown. The tomographic reconstruction was done using the Minerva framework.

E. The Minerva framework

Minerva is a generic software framework for Bayesian scientific modeling and data analysis [34]. It uses the concept of Bayesian graphical models [45] to fully describe forward models, statistical and systematic uncertainties, regularizing priors and their dependencies on each other. Several hundred modules (nodes in the graphical models) have been written for different aspects of plasma modeling, such as representation of fields, los integration, power coil modeling, Biot-Savart, bremsstrahlung, neutral beam attenuation/penetration, equilibrium, 2D/3D flux coordinate transformations etc. About 20 diagnostic systems have been modeled in detail in Minerva which have been used and tested at JET, MAST, TJ-II, TCV, KSTAR, ASDEX Upgrade and W7-X. The Bayesian approach in combination with the Minerva architecture allows multiple diagnostics to be easily combined to give evidence on physics parameters (such as a density profile) from multiple diagnostics jointly, which can significantly increase the accuracy of reconstructions [46,47]. At W7-X it is the default system for modeling and analyzing diagnostic data, making W7-X the first experiment that has a generic modeling and analysis framework in place. An important aspect of the framework is the separation of modeling from inference algorithms, and so after a model has been created a number of different generic inference schemes, such as linear and nonlinear optimization to find the Maximum a Posteriori (MAP) solution, or Markov Chain Monte Carlo (MCMC) schemes to find full non-Gaussian error distributions can be applied, allowing the physicist to concentrate on the actual model rather than how to infer parameters based on that model. Minerva is able to call legacy codes (for example for 3D equilibria or ECE ray tracing) as separate services running on a virtual cloud using a service oriented architecture [34,48].

III. SUMMARY

The optimized superconducting stellarator Wendelstein 7-X has been successfully commissioned in 2015. The first experimental campaign with five uncooled graphite inboard limiters defining the LCFS has been conducted between December 2015 and March 2016 allowing the integral commissioning of all machine components and installed diagnostics. More than 20 diagnostic systems have been put into operation and delivered in almost all cases reliable measurements allowing many physics investigations in ~1000 discharges of up to 6 sec. length and with plasma temperatures and densities exceeding predicted values from simulations.

This work has been carried out within the framework of the EUROfusion Consortium and has received funding from the Euratom research and training programme 2014-2018 under grant agreement No 633053. The views and opinions expressed herein do not necessarily reflect those of the European Commission. This work was funded in part by the Department of Energy under grants DE-SC0014210. This scientific work was also partly supported by Polish Ministry of Science and Higher Education within the framework of the scientific financial

resources in the years 2015 and 2016 allocated for the realization of the international co-financed project.

IV. REFERENCES AND FOOTNOTES

- 1 T. Sunn Pedersen *et al.*, Nucl. Fusion **55**, 126001 (2015).
- 2 R. König *et al.*, Journal of Instrumentation **10**, (2015).
- 3 B. Wiegel *et al.*, Radiat. Prot. Dosim. **161**, 326 (2014).
- 4 D. Moseev *et al.*, Absolute calibration of sniffer probes on Wendelstein 7-X, submitted to Rev. Sci. Instrum. (2016).
- 5 M. Endler *et al.*, Fusion Engineering and Design **100**, 468 (2015).
- 6 M. Hirsch *et al.*, Journal of Instrumentation **10**, (2015).
- 7 T. Windisch *et al.*, in 42nd EPS Confer. on Plasma Phys. **39E**, (2015).
- 8 A. Kraemer-Flecken *et al.*, Rev. Sci. Instrum. **81**, 113502 (2010).
- 9 H.-J. Hartfuss, R. König and A. Werner, Plasma Phys. Control. Fusion **48**, R83 (2006).
- 10 R. König *et al.*, Rev. Sci. Instrum. **83**, 10D730 (2012).
- 11 M. Otte *et al.*, Plasma Phys. Control. Fusion **58**, 064003 (2016).
- 12 E. Pasch *et al.*, Rev. Sci. Instrum., this conference (2016).
- 13 P. Kornejew, H. Trimino Mora and M. Hirsch, Single channel interferometer for the stellarator Wendelstein 7-X, to be published.
- 14 M. Hirsch *et al.*, 1st EPS Conference on Plasma Diagnostics, Frascati (Rome) Italy (2015).
- 15 D. Wagner *et al.*, J Infrared Milli Terahz Waves **32**, 1424 (2011).
- 16 G. Kocsis *et al.*, Fusion Engineering and Design **96-97**, 808 (2015).
- 17 G. Haas and H.-S. Bosch, Vacuum **51**, 39 (1998).
- 18 K. Flesch *et al.*, Rev. Sci. Instrum., this conference (2016).
- 19 U. Wenzel *et al.*, On the neutral density in the Wendelstein-7X stellarator, to be published.
- 20 G. A. Wurden, L. Stephey, C. Biedermann, M. W. Jakubowski, J. P. Dunn, M. Gamradt, and the W7-X Team, Rev. Sci. Instrum., this conference (2016).
- 21 L. Stephey *et al.*, Rev. Sci. Instrum., this conference (2016).
- 22 A. Herrmann, W. Junker, K. Günther, S. Bosch, M. Kaufmann, J. Neuhauser, G. Pautasso, T. Richter, and R. Schneider, Plasma Phys. Control. Fusion **37**, 17 (1995).
- 23 R. J. Colchin *et al.*, Rev. Sci. Instrum. **74**, 3 (2003).
- 24 H. Frerichs *et al.*, Rev. Sci. Instrum., this conference (2016).
- 25 M. Griener *et al.*, Rev. Sci. Instrum., this conference (2016).
- 26 F. Effenberg *et al.*, Numerical investigation of plasma edge transport and limiter heat fluxes in Wendelstein 7-X startup plasmas with EMC3-Eirene, submitted to Nuclear Fusion (2016).
- 27 T. Barbui *et al.*, Rev. Sci. Instrum., this conference (2016).
- 28 M. Krychowiak, M. Brix, D. Dodt, Y. Feng, R. Koenig, O. Schmitz, J. Svensson and R. Wolf, Plasma Phys. Control. Fusion **53**, 035019 (2011).
- 29 P. Drews *et al.*, in 43rd EPS Confer. on Plasma Phys. (2016).
- 30 N.A. Pablant *et al.*, in 41st EPS Confer. on Plasma Phys. **38F**, (2014).
- 31 A. Langenberg, J. Svensson, H. Thomsen, O. Marchuk, N. A. Pablant, R. Burhenn, R. C. Wolf, Fusion Sci. Technol. **69**, 560 (2016).
- 32 A. Langenberg *et al.*, in 41st EPS Confer. on Plasma Phys. **38F**, (2014).
- 33 G. Bertschinger *et al.*, Rev. Sci. Instrum. **75**, 3727 (2004).
- 34 J. Svensson and A. Werner, in International Symposium on Intelligent Signal Processing-WISP, 955 (2007).
- 35 N.A. Pablant *et al.* in 43rd EPS Confer. on Plasma Phys. (2016).
- 36 A. Langenberg *et al.* in 43rd EPS Confer. on Plasma Phys. (2016).
- 37 W. Biel, A. Greiche, R. Burhenn, E. Jourdain, and D. Lepere, Rev. Sci. Instrum. **75**, 3268 (2004).
- 38 W. Biel, G. Bertschinger, R. Burhenn, R. König, and E. Jourdain, Rev. Sci. Instrum. **77**, 10F305 (2006).
- 39 H. Thomsen *et al.*, J. Instr. **10**, P10015 (2015).
- 40 M. Kubkowska *et al.*, J. Instr. **10**, P10016 (2015).
- 41 S. Jablonski, J. Instr. **10**, P10021 (2015).
- 42 D. Zhang *et al.*, Rev. Sci. Instrum. **81**, 10E134 (2010).
- 43 D. Zhang *et al.*, in 38th EPS Confer. on Plasma Phys. **35G**, (2011).
- 44 J. Svensson, Nonparametric tomography using Gaussian Processes, JET Internal report, EFDA-JET-PR(11) 24, 2011.
- 45 S. L. Lauritzen, *Graphical Models*, Oxford Statistical Science Series, 1996.
- 46 O. Ford *et al.*, in 36th EPS Confer. on Plasma Phys. **33E**, (2009).
- 47 J. Svensson *et al.*, in 37th EPS Confer. on Plasma Phys. **34A**, (2010).
- 48 A. Werner *et al.*, Fusion Engineering and Design **85**, 394 (2010).